remote sensing

MDPI

Article

Where Himalayan Forests Are More (or Less) Complex than Their Height Suggests: An Uncertainty-Aware GEDI Indicator for Monitoring and Management

Niti B. Mishra * and Gargi Chaudhuri

Department of Geography & Environmental Science, University of Wisconsin-La Crosse, La Crosse, WI 54601, USA; gchaudhuri@uwlax.edu

* Correspondence: nmishra@uwlax.edu; Tel.: +1-608-785-8334

Highlights

What are the main findings?

- Developed an uncertainty-aware GEDI indicator of forest structural complexity relative to canopy height across the Hindu Kush Himalaya and mapped areas of higher- and lower-than-expected complexity at 1 km scale.
- Found strong, coherent organization of complexity anomalies along elevation/treeline-relevant belts and persistent biogeographic differences among ecoregions even after stratified adjustment for elevation and mean annual precipitation.

What are the implications of the main findings?

- Provides a scalable, uncertainty-characterized framework to move beyond canopy height and identify landscapes where habitat- and microclimate-relevant vertical structure may deviate from expectations.
- Supports targeted field validation and monitoring prioritization (e.g., by ecoregion, protected area status, and elevational belts) using repeatable spaceborne LiDAR metrics for data-scarce mountain forests.

Abstract

Forest structural complexity underpins habitat quality, microclimate buffering, and resilience, yet it remains poorly characterized across the Hindu Kush Himalaya (HKH) where field inventories and airborne LiDAR are difficult to scale across rugged terrain. Conservation planning and protected-area evaluation in the HKH therefore often rely on canopy height or cover proxies that do not directly represent vertical structural organization. Here we develop a repeatable, uncertainty-aware indicator of forest structural complexity from GEDI waveform LiDAR using the Waveform Structural Complexity Index (WSCI) and its prediction intervals. We first define a conservative analysis footprint ("trustable pixels") by combining a woody-vegetation screen with minimum GEDI sampling support and canopy-stature plausibility, and by excluding the highest-uncertainty tail using a relative prediction-interval criterion. To separate complexity from canopy height, we model the HKH-wide expected WSCI–RH98 relationship and map height-normalized excess complexity (observed minus expected), identifying structural complexity hotspots and coldspots as the upper and lower tails of the excess distribution. Anomaly patterns are strongly organized along elevation and treeline-relevant belts and show coherent departures among ecoregions that persist after stratified adjustment for elevation and mean annual precipitation, indicating additional controls beyond broad environmental gradients. Protected areas exhibit systematically lower hotspot prevalence than surrounding landscapes, and

Check for updates

Academic Editors: Jan Komarek and Marlena Kycko

Received: 6 March 2026
Revised: 7 April 2026
Accepted: 15 April 2026
Published: 17 April 2026

Copyright: © 2026 by the authors. Licensee MDPI, Basel, Switzerland. This article is an open access article distributed under the terms and conditions of the Creative Commons Attribution (CC BY) license.

within-elevation comparisons suggest this association is not explained by elevation alone, highlighting the need to interpret protected-area signals in the context of placement and land-use pressure. Overall, the anomaly atlas provides an operational indicator framework to stratify monitoring, prioritize field validation, and support the landscape-scale assessment of structural conditions beyond canopy height across one of the world's most critical mountain forest systems.

Keywords: conservation monitoring; forest structure; structural complexity; GEDI; spaceborne LiDAR; mountain forests; protected areas; ecoregions; Hindu Kush Himalaya; uncertainty

1. Introduction

Mountain forests of the Hindu Kush Himalaya (HKH) support globally significant biodiversity [1,2], regulate regional hydrology [3], and provide ecosystem services to hundreds of millions of people downstream [4,5]. The HKH also spans extreme climatic and topographic gradients, from monsoon-influenced, species-rich forests to cold, high-elevation systems approaching the treeline, creating sharp transitions in forest composition, stature, and disturbance regimes [1,6]. Despite this ecological importance, the spatial distribution of forest structural complexity across the HKH remains poorly quantified at regional-to-pan-HKH scales [7], largely because field inventories and airborne LiDAR campaigns are spatially sparse and logistically difficult in rugged terrain [8].

Forest structural complexity—the three-dimensional arrangement of vegetation elements in space—has been repeatedly linked to ecosystem function and habitat quality [9,10]. Structurally complex forests can support higher niche diversity, alter microclimates, and provide critical habitat features (e.g., vertical layering, canopy gaps, and heterogeneous crown architecture) that influence species richness and occupancy [10–12]. Empirical work has shown that complexity can covary with productivity and carbon dynamics [13], and that management and protection status can measurably influence structural complexity [14] and associated habitat suitability in forests [15]. At the same time, complexity is not synonymous with canopy height: tall forests can be structurally simple (e.g., closed-canopy stands with limited understory) while moderate-height forests can be structurally complex (e.g., multi-layered stands with gaps and heterogeneous crowns) [9,16,17]. This distinction matters in mountainous regions where elevation, moisture availability, and disturbance history jointly shape canopy height, canopy cover, and vertical layering in ways that may decouple height from ecological complexity [18–20].

Remote sensing has transformed our ability to map forest structure, but most HKH-scale products emphasize canopy height [21], greenness [22], or canopy cover [23] rather than three-dimensional complexity [24]. Optical time series (e.g., MODIS) are powerful for tracking phenology [25] and disturbance [26] but provide limited direct information on vertical structure. Airborne LiDAR scanning (ALS) can quantify fine-scale canopy architecture and vertical complexity, but broad HKH coverage is unrealistic with either Unoccupied Aerial Vehicle (UAV)-based [27] or aircraft-based campaigns [28]. As a result, key ecological questions remain unresolved at HKH scale: Where are forests unusually complex relative to their canopy height? Where are structurally simplified forests concentrated, and do these align with biogeographic gradients, treeline belts, or human pressure? Are protected areas associated with systematically different structural complexity outcomes after accounting for biophysical context?

The GEDI (Global Ecosystem Dynamics Investigation) spaceborne lidar mission provides a unique opportunity to address these gaps by sampling vertical forest structure globally with waveform lidar footprints [29]. GEDI's relative height (RH) metrics and derived products have enabled regional and global estimates of canopy height and biomass [30,31], and recent work has expanded waveform-based inference beyond height to include structural complexity [24]. In particular, the Waveform Structural Complexity Index (WSCI) was developed to estimate three-dimensional forest structural complexity directly from GEDI waveform information, leveraging large training datasets where GEDI footprints overlap ALS point clouds. In this framework, plant functional type–specific models use GEDI RH percentile profiles to predict ALS-derived structural complexity at the footprint scale, and these footprint predictions can then be summarized to gridded products suitable for regional mapping and analysis [24]. Importantly, this modeling approach is accompanied by prediction intervals that quantify uncertainty in WSCI estimates, enabling uncertainty-aware filtering and sensitivity analyses, an essential feature for applications in heterogeneous, mountainous landscapes [32].

However, translating waveform-derived complexity into robust ecological inference across a vast and diverse region like the HKH requires careful treatment of data quality, land-cover mixing, and spatially varying uncertainty. First, GEDI sampling density is uneven in space, and gridded summaries may reflect relatively few footprints in some locations [33,34]. Second, land-cover heterogeneity at 1 km resolution can yield grid cells where non-forest land covers dominate but a subset of forested footprints contribute complexity estimates, potentially producing ecologically confusing patterns, if not explicitly masked, to woody vegetation [31]. Third, prediction intervals for WSCI are heteroscedastic, meaning uncertainty is not uniform across the range of complexity or across forest types; this makes a single uncertainty cutoff difficult to justify over large regions without inducing spatial bias. These issues motivate an approach that (i) defines a defensible analysis mask for woody vegetation and minimum sampling density, (ii) filters uncertainty using relative rather than absolute thresholds, and (iii) focuses interpretation on anomalies—areas that are more (or less) complex than expected given canopy height—rather than raw complexity alone.

Accordingly, in this study we ask: (1) Where across the HKH do GEDI-derived WSCI estimates provide a defensible, uncertainty-aware "trustable" footprint for inference, and how do WSCI mean, uncertainty, and GEDI sampling density vary spatially within that footprint? (2) What is the HKH-wide expected relationship between structural complexity (WSCI) and canopy height, and where do forests deviate from this baseline, exhibiting "excess complexity" (higher-than-expected) or "structural simplification" (lower-than-expected) after accounting for height? (3) Do hotspots and coldspots show coherent organization along major biogeographic gradients (ecoregions/biomes), across protection status (inside vs. outside WDPA protected areas), and across elevation bands spanning upper-montane and treeline-relevant belts? The focal indicator is height-normalized vertical forest structural organization (i.e., structural complexity beyond canopy stature), expressed as an uncertainty-screened anomaly indicator derived from GEDI waveforms.

2. Methods

2.1. Study Region

The study area is the Hindu Kush Himalaya (HKH), which spans ~3500 km from Afghanistan in the west to Myanmar in the east across all or part of eight countries (Figure 1) and has a total estimated area of 3,441,719 km^2 [35]. The HKH contains extreme elevational relief and strong climatic gradients (including monsoon–westerly influences and pronounced rain-shadow effects) that drive rapid turnover in vegetation, from subtropi-

cal and temperate forests to subalpine forests and treeline ecotones (Figure 1b) [1,36,37]. The HKH is a comparatively densely populated mountain landscape [38] where land use change [39] and resource demand further interact with these biogeographic and environmental gradients to produce heterogeneous canopy height, canopy cover, and vertical layering over short distances [5]. These are conditions under which canopy height may be partly decoupled from ecological complexity which is central to interpreting GEDI-derived three-dimensional structural complexity across the region. The HKH is also a global biodiversity priority region that includes four global biodiversity hotspots and twelve Global 200 ecoregions, but ecological representation in protection is uneven [40]. A recent regional assessment reports 575 protected areas covering 40.17% of the HKH, while substantial fractions of ecoregions and other key biodiversity features remain outside protected areas [41], making the region well suited for evaluating how complexity patterns relate to biogeographic context and protection status. The HKH is also experiencing acute environmental pressures as mountain warming is amplified relative to global averages [42] with shifting monsoon behavior [43] leading to species extinction and multi-hard risks that can cascade across borders [44].

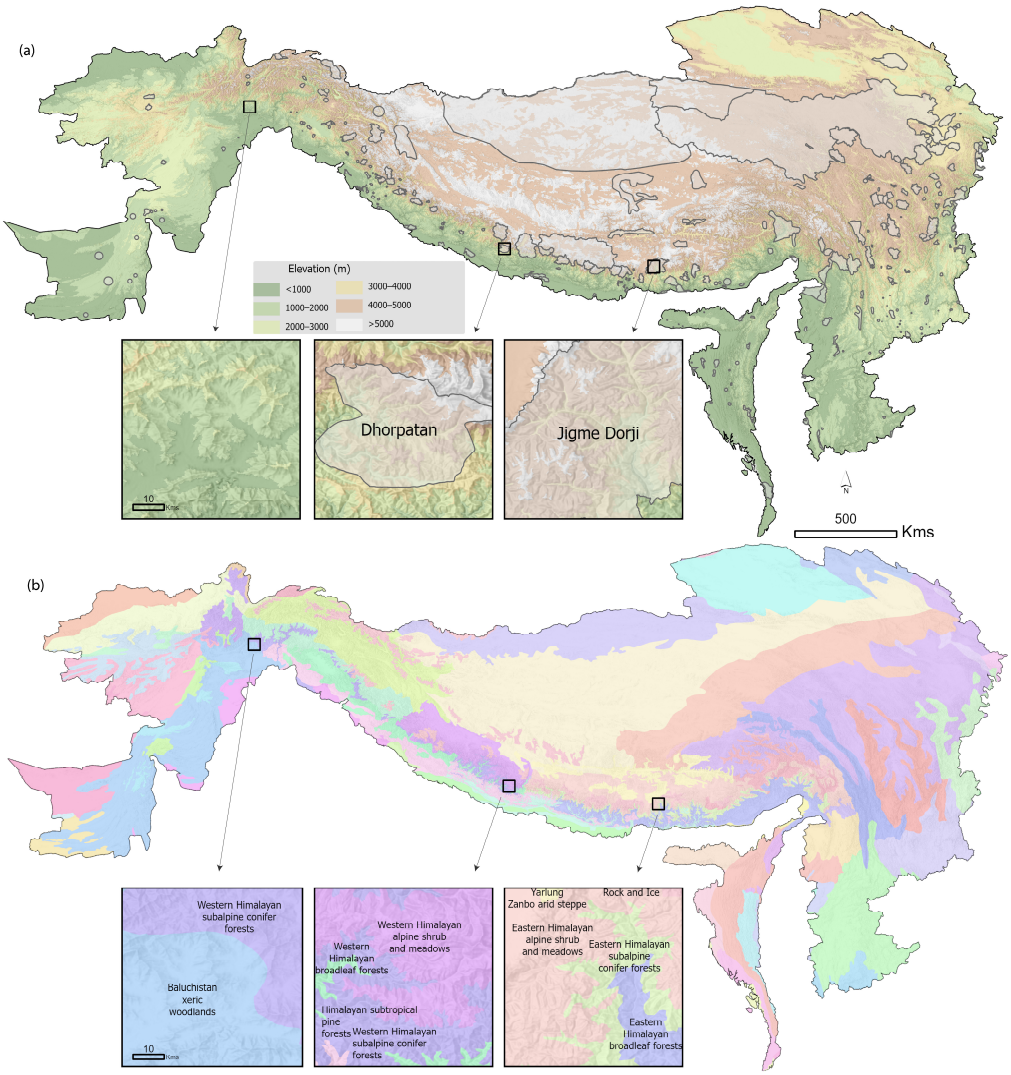

Figure 1. (**a**) HKH study boundary overlaid six elevation classes and protected areas are shown as gray outlines. Insets provide examples of local terrain context and protected-area geometry and (**b**) WWF/RESOLVE terrestrial ecoregions within the HKH boundary, illustrating strong biogeographic turnover along the arc.

2.2. Data Sources

2.2.1. GEDI/WSCI Products

We used the Waveform Structural Complexity Index (WSCI) derived from NASA's Global Ecosystem Dynamics Investigation (GEDI) lidar waveforms [45]. WSCI is a waveform-based metric designed to summarize 3D structural complexity at GEDI footprint scale using information contained in GEDI relative height (RH) metrics, and it is distributed along with an uncertainty estimate based on conformal prediction (prediction intervals). For HKH-scale analysis, we used the published 1 km gridded WSCI product with prediction interval magnitude [32]. WSCI is first estimated at the GEDI footprint scale and then summarized to a 1 km grid. The gridded product is intended to provide spatially consistent regional patterns while retaining a traceable link back to footprint-scale GEDI information. We chose this product rather than the newer 25 m WSCI Fusion product because our objective was to analyze a conservative, observation-linked regional indicator derived directly from gridded GEDI footprint summaries and to pair it consistently with 1 km RH98, countf, woody-cover, elevation, and MAP layers.

2.2.2. GEDI RH Metrics and Sampling Density (Countf)

To model "expected" WSCI as a function of canopy height structure, we used the gridded GEDI RH98 product (1 km resolution) that provides (i) RH98 (median) which is a robust proxy for upper-canopy height/stature and (ii) countf which is a sampling-density indicator containing the number of GEDI footprints contributing to the gridded estimate. We treated countf as a reliability screen, because RH summaries can be unstable when derived from very few footprints per 1 km cell [46], especially in rugged HKH terrain where GEDI sampling can be spatially uneven [34]. Accordingly, we required a minimum countf threshold ($\geq$10) and a minimum RH98 ($\geq$5 m) threshold to exclude cells where RH98 is likely to represent noise, sparse vegetation, or poor sampling.

2.2.3. Woody/Forest Mask

To focus interpretation on natural woody vegetation, we used a custom 1 km woody mask built from Copernicus Global Land Service (CGLS) fractional land-cover information [46]. The mask was constructed by aggregating the fractional cover information to the WSCI 1 km grid and applying thresholds that retain pixels dominated by woody vegetation while excluding croplands and other non-woody covers. Fractional cover layers for tree cover, shrub cover, snow/ice, water, urban, and cropland were first aggregated from 100 m to the WSCI 1 km grid using mean proportions. We then defined a pixel as woody-dominant if the combined tree + shrub fraction was at least 0.40, while snow, water, urban, and crop fractions were constrained to $\leq$0.05, $\leq$0.05, $\leq$0.10, and $\leq$0.05, respectively. This conservative mask was designed to exclude mixed pixels in which a small amount of woody cover could otherwise strongly influence the 1 km mean WSCI signal. This analysis mask was applied before: (i) computing the expected WSCI model, and (ii) structural complexity hotspot/coldspot patterns. This made sure that downstream results reflect forested/woody structures rather than land-cover artifacts.

2.2.4. Ecoregions and Protected Areas (PAs)

To stratify structural complexity anomalies by biogeography, we used the RESOLVE/WWF ecoregions (2017 update) dataset, which maps global terrestrial ecoregions and is widely used for biodiversity and conservation analyses. These units are ultimately based on the "Terrestrial Ecoregions of the World" framework [47]. To assess protection effects, we used the World Database on Protected Areas (WDPA) as curated by UNEP-WCMC and IUCN/Protected Planet [48]. We intersected WDPA polygons with the HKH

analysis mask and summarized WSCI, excess, and structural complexity hotspot/coldspot frequencies inside vs. outside PAs and, where needed, within ecoregion strata.

2.2.5. Elevation

To contextualize results relative to topographic constraints and treeline-relevant gradients, we used a SRTM DEM [49] and aggregated elevation to the 1 km WSCI grid using mean elevation per 1 km pixel. The DEM was used only for stratified summaries and charts (e.g., structural complexity hotspot/coldspot frequency by elevation band), not as an input to the expected-WSCI model in the baseline analysis. The SRTM product characteristics are documented in the Earth Engine data catalog [50].

2.2.6. Mean Annual Precipitation (MAP)

To characterize broad hydroclimatic context across the HKH, we used mean annual precipitation (MAP) from the WorldClim v1 bioclimatic variables (BIO) dataset, specifically BIO12 (annual precipitation; mm) [51]. The WorldClim v1 BIO layers represent long-term climate normals from approximately 1960–1990 which are available in Google Earth Engine. We clipped BIO12 to the HKH bounds and aggregated MAP to the WSCI 1 km grid using a mean reducer (i.e., average precipitation within each 1 km WSCI cell) to ensure spatial alignment with the gridded GEDI/WSCI products used in subsequent stratified analyses.

2.3. Overview of Analysis

The overall workflow is summarized in Figure 2. All analyses were conducted on a consistent 1 km grid across the HKH in Google Earth Engine. We first defined a conservative analysis footprint by combining the woody-dominant mask, GEDI canopy-height and sampling-support filters, WSCI availability, and an uncertainty screen (Figure 3). Within this footprint, we then modeled the expected relationship between WSCI and RH98 to derive height-normalized indicator anomalies. These anomaly values were subsequently classified into upper- and lower-tail categories and used for stratified analyses across elevation, ecoregions, and protected-area status. The detailed implementation of each step is described in Sections 2.4–2.7.

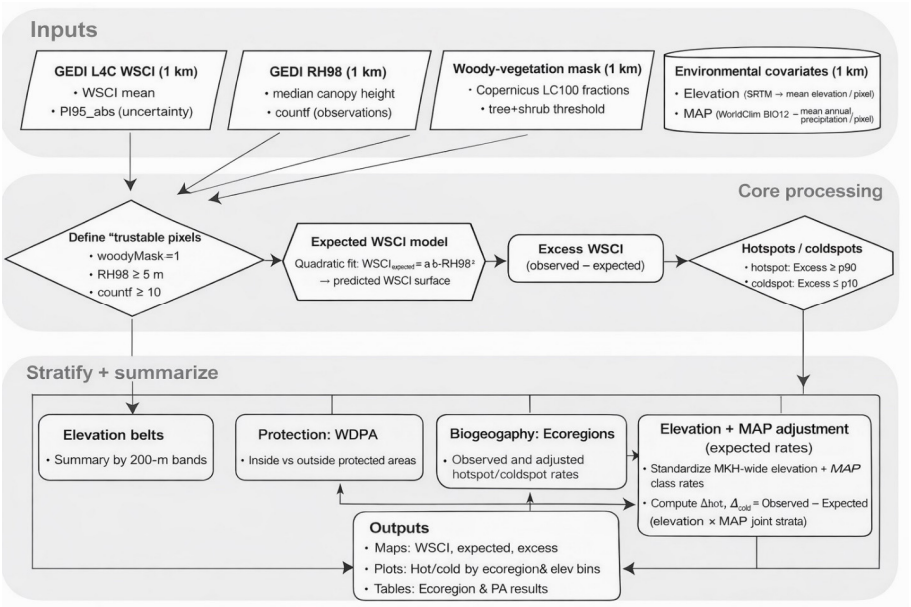

Figure 2. Workflow schematic for mapping and interpreting forest structural complexity anomalies across the HKH.

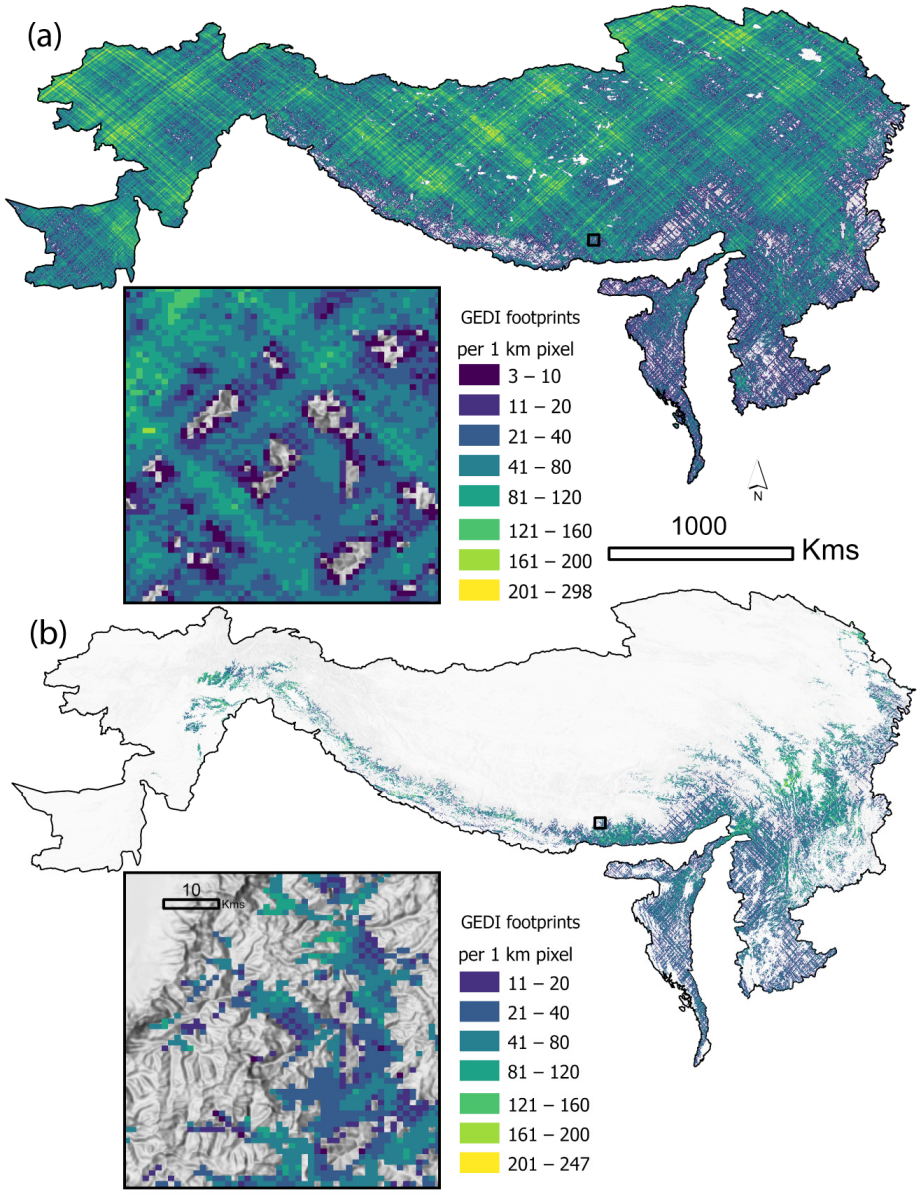

Figure 3. GEDI sampling density and progressive filtering for "indicator footprint" 1 km pixels across the HKH; (**a**) unfiltered GEDI footprint density (countf) per 1 km pixel and (**b**) pixels retained after the full set of "indicator footprint" filters.

2.4. Uncertainty Characterization and Indicator Screening

The gridded WSCI product includes an uncertainty layer representing the magnitude of the prediction interval around the mean estimate. To account for heterogeneity in the magnitude of WSCI values across vegetation types and environments, we defined uncertainty in relative rather than absolute terms:

$$\mathbf{relPI} = \frac{\mathbf{PI}_{abs}}{\mathbf{WSCI}_{mean}}$$

where PI_{abs} is the prediction-interval magnitude provided with the WSCI grid and $WSCI_{mean}$ is the mean WSCI estimate for the same pixel. A single fixed uncertainty cutoff (e.g., PI < constant) is difficult to justify over a domain as diverse as the HKH because uncertainty is not spatially uniform and may vary systematically by biome, canopy structure, and sampling density. A global fixed cutoff can therefore induce spatial bias by disproportionately excluding certain forest types or regions. To avoid this, we adopted a percentile-based

cutoff computed directly from the HKH distribution of relPI. Our primary uncertainty rule retained pixels with:

$$\mathbf{relPI} \leq \boldsymbol{P_{90}}\mathbf{rel}\boldsymbol{PI}$$

i.e., we excluded the highest-uncertainty tail while retaining the majority of pixels. In the HKH analysis, the resulting threshold was approximately $relPI_{90}$ = 0.278 (computed from the masked HKH distribution).

2.5. Height-Normalization to Isolate Structural Organization Beyond Canopy Height

To identify locations where forest structural complexity is unusually high or low relative to canopy stature, we estimated an expected WSCI or "indicator baseline" as a function of canopy height and then analyzed deviations from this baseline. We modeled the indicator baseline as a quadratic function of RH98:

$$\hat{\boldsymbol{WSCI}} = \boldsymbol{a} + \boldsymbol{bH} + \boldsymbol{cH^2}$$

where H is the 1 km RH98 median and a, b, c are regression coefficients estimated using ordinary least squares. The quadratic form was selected as a minimal nonlinear model capable of capturing monotonic increases at low-to-moderate heights and curvature (e.g., saturation or flattening) at higher heights without overfitting.

As the HKH contains millions of 1 km pixels, coefficients were estimated using a large random sample drawn from the trustable indicator footprint. The fitted model was then applied to all pixels in the footprint to generate a wall-to-wall indicator baseline surface. We defined the anomaly ("Indicator anomalies") as:

$$\textbf{Indicator anomalies} = \mathbf{WSCI_{obs}} - \widehat{\mathbf{WSCI}}$$

Positive excess values indicate structural complexity greater than expected for the observed canopy height, while negative values indicate lower-than-expected complexity. As a diagnostic, we evaluated the association between RH98 and Indicator anomalies to confirm that the anomaly surface does not retain a strong dependence on canopy height (i.e., excess is not simply a transformed height map).

2.6. Indicator Classification (Tails of Excess Complexity)

Structural complexity hotspots and coldspots were defined from the empirical distribution of indicator anomaly values within the trustable indicator footprint. We used a percentile-based classification, where structural complexity hotspots were defined as pixels with indicator anomalies $\geq$ p90 of the masked excess distribution, whereas structural complexity coldspots were pixels with indicator anomalies $\leq$ p10 of the masked excess distribution. Percentile thresholds were estimated from a large random sample of masked excess values to ensure stable estimates at HKH scale.

2.7. Stratified Analyses

We examined how structural complexity anomalies vary across elevation/treeline-relevant gradients, biogeographic units (ecoregions), and protection status, including variation in structural complexity hotspot and coldspot frequency. Elevation was derived from a global DEM and aggregated to the WSCI 1 km grid (mean elevation per pixel). We binned elevation in fixed-width increments (e.g., 200 m bins) and computed for each bin: (i) structural complexity hotspot frequency (hotspot pixels/total footprint pixels), (ii) structural complexity coldspot frequency, and (iii) mean indicator anomaly (and optionally mean RH98). These summaries characterize how anomalies vary along the elevational gradient relevant to treeline-zone transitions and high-elevation constraints.

Besides elevation, we intersected the analysis footprint with the RESOLVE/WWF terrestrial ecoregions dataset and computed ecoregion-level summaries including masked area, mean observed WSCI, mean indicator anomaly, hotspot percentage, and coldspot percentage. To keep presentation tractable, we focused on a shortlist of dominant ecoregions that together captured most of the masked HKH footprint (excluding xeric/non-forest systems where appropriate). Percentages were computed on an area-weighted basis over the 1 km grid.

As structural complexity hotspot/coldspot frequency varies strongly with elevation across the HKH, direct comparisons of raw hotspot and coldspot fractions among ecoregions can be confounded by differences in each ecoregion's elevation distribution. To isolate the ecoregion-specific signal, we computed elevation- and precipitation-adjusted expectations using a stratified standardization approach. First, we summarized HKH-wide baseline hotspot and coldspot rates by 200 m elevation bands (b), using the final analysis mask (Indicator coverage/footprint) and the hotspot/coldspot classification derived from indicator anomalies. For each elevation band, we calculated the HKH-wide hotspot rate $HotRate_{HKH,b}$ and $ColdRate_{HKH,b}$ as the proportion of masked pixels in that band classified as hotspot or coldspot, respectively. Second, for each ecoregion e, we computed its elevation-band composition $w_{e,b}$, defined as the fraction of that ecoregion's masked pixels that fall within elevation band b (so $\sum_b w_{e,b} = 1$). We then computed elevation-expected hotspot and coldspot rates for each ecoregion as weighted averages of the HKH-wide elevation-band rates:

$$ExpectedHot_e = \sum_b w_{e,b} \mathbf{HotRate}_{KHK,b}$$

$$ExpectedCold_e = \sum_b w_{e,b} \mathbf{ColdRate}_{KHK,b}$$

To additionally control for precipitation, we extended the approach by incorporating a mean annual precipitation (MAP) stratum. Specifically, we computed HKH-wide structural complexity hotspot/coldspot rates within joint strata of elevation band b and precipitation class p, yielding $\mathbf{HotRate}_{KHK,b,p}$ and $\mathbf{ColdRate}_{KHK,b,p}$. For each ecoregion, we computed weights $w_{e,b,p}$ based on the proportion of masked pixels in each joint stratum. Elevation + MAP, expected rates were then:

$$ExpectedHot_e = \sum_b \sum_p w_{e,b,p} \mathbf{HotRate}_{KHK,b,p'}$$

$$ExpectedCold_e = \sum_b \sum_p w_{e,b,p} \mathbf{ColdRate}_{KHK,b,p.}$$

Finally, we quantified each ecoregion's adjusted deviation (residual) as the difference between observed and expected rates:

$$\Delta \mathbf{hot}_e = \mathbf{ObservedHot}_e - \mathbf{ExpectedHot}_e$$

$$\Delta \mathbf{cold}_e = \mathbf{ObservedCold}_e - \mathbf{ExpectedCold}_e$$

Positive $\Delta \mathbf{hot}_e$ indicates that an ecoregion contains more hotspots than expected given its elevation (and MAP) distribution, whereas negative values indicate a hotspot deficit. Analogous interpretation applies to $\Delta \mathbf{cold}_e$. This framework enables fairer biogeographic comparisons by removing first-order compositional effects of elevation and precipitation while retaining ecologically meaningful residual structure.

Besides biogeographic controls, to access the influence of area protection status on hotspot and coldspot distribution, protected-area polygons from WDPA were intersected with the HKH domain and rasterized to the 1 km grid to classify pixels as protected vs. non-protected. We computed inside/outside differences in mean indicator anomaly and

structural complexity hotspot/coldspot frequencies (i) HKH-wide and (ii) within ecoregions to control for biogeographic differences. As analyses are conducted on a 1 km grid, "partial" pixel overlaps with protected-area boundaries are discretized by the rasterization rule (e.g., pixel-center assignment), and results are interpreted as regional-scale shifts rather than boundary-level effects.

3. Results

3.1. HKH WSCI Map and Uncertainty Patterns

Across the HKH, the woody-filtered "analysis footprint" retained ~590,002 km^2 of "indicator footprint" forested area after applying the woody mask and GEDI sampling-density and quality filters. Within this footprint, woody-masked WSCI mean values showed a relatively tight distribution compared to unfiltered maps, with a median of ~9.28, and a 2–98% range of ~8.21 to ~10.55 (Figure 4). This constrained range is consistent with the analysis focusing on forested pixels that have sufficient GEDI support and acceptable waveform-model uncertainty.

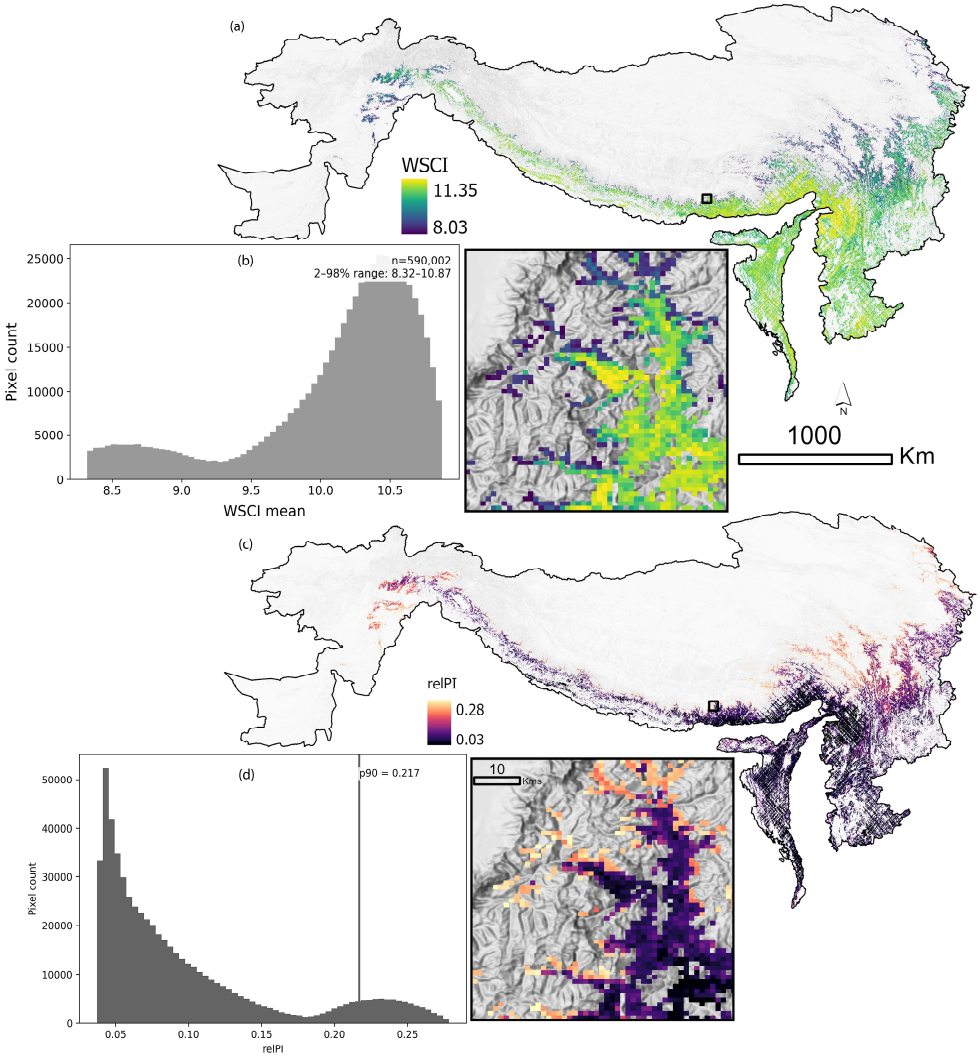

Figure 4. Spatial patterns in (**a**) WSCI and (**c**) uncertainty across the HKH after applying the analysis ("Indicator coverage/footprint") mask; (**b**) shows frequency distribution of masked WSCI mean values (n = 590,002 pixels) and (**d**) shows distribution of relPI values within the masked footprint; the vertical line marks the adopted uncertainty cutoff (p90 = 0.278), illustrating the long right tail of higher-uncertainty pixels that are excluded by the percentile-based filter.

Uncertainty screening based on relative prediction interval (relPI; PI normalized by the predicted/mean value) removed the highest-uncertainty tail of pixels. Using the HKH-wide percentile strategy, the relPI threshold was set at the 90th percentile (p90 ≈ 0.278), which provides a region-consistent way to exclude the most uncertain grid cells while preserving broad coverage (Figure 4c,d).

3.2. Indicator Baseline: Expected WSCI–RH98 Relationship

Having established a conservative footprint for inference and characterized uncertainty within it, we next modeled the HKH-wide expected relationship between WSCI and canopy stature to separate height-driven structure from 'excess' complexity. To normalize structural complexity for canopy stature, indicator baseline was modeled as a quadratic function of RH98 (median canopy height proxy) using a random sample from the indicator footprint (n = 16,646 sampled pixels). The fitted relationship was:

$$\widehat{WSCI} = a + b * RH98 + c * RH98^2$$

with coefficients a = 7.357, b = 0.174, c = −0.00223 (Figure 5a). Model fit was strong at HKH scale (R^2 = 0.746) with RMSE ≈ 0.335 WSCI units, indicating that canopy height explains a substantial fraction of large-scale variation in WSCI while still leaving meaningful residual structure (the "excess" signal) for ecological interpretation. The negative quadratic term implies a concave relationship (increasing WSCI with height up to a peak around ~39 m, then flattening/declining), consistent with the idea that waveform-inferred complexity saturates once forests reach mature canopy heights and additional height contributes less to within-footprint vertical heterogeneity.

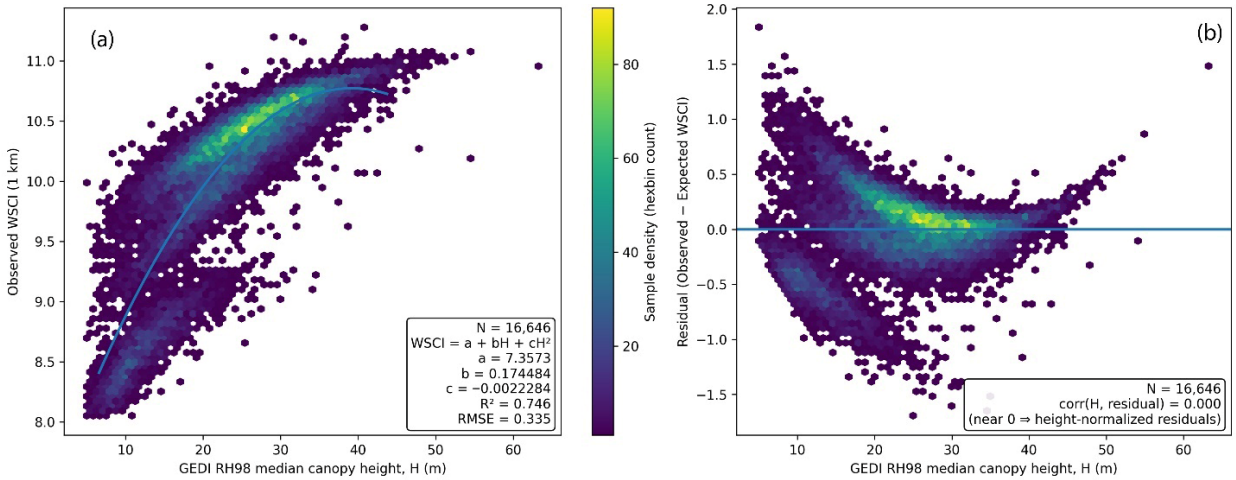

Figure 5. (**a**) Height-normalized "expected" WSCI model and (**b**) residual diagnostics for defining excess structural complexity across the HKH.

3.3. Spatial Hotspots/Coldspots

Indicator anomalies were computed as Observed−Expected, yielding a residual complexity surface that is explicitly "height-normalized." The HKH-wide excess distribution was centered near zero (mean approximately −0.001; median ~0.023), with percentile thresholds of approximately p10 ≈ −0.430 and p90 ≈ +0.367 used to define coldspots and hotspots, respectively. By construction, hotspots and coldspots each represent roughly the most extreme ~10% tails of the trustable indicator footprint (Figure 6).

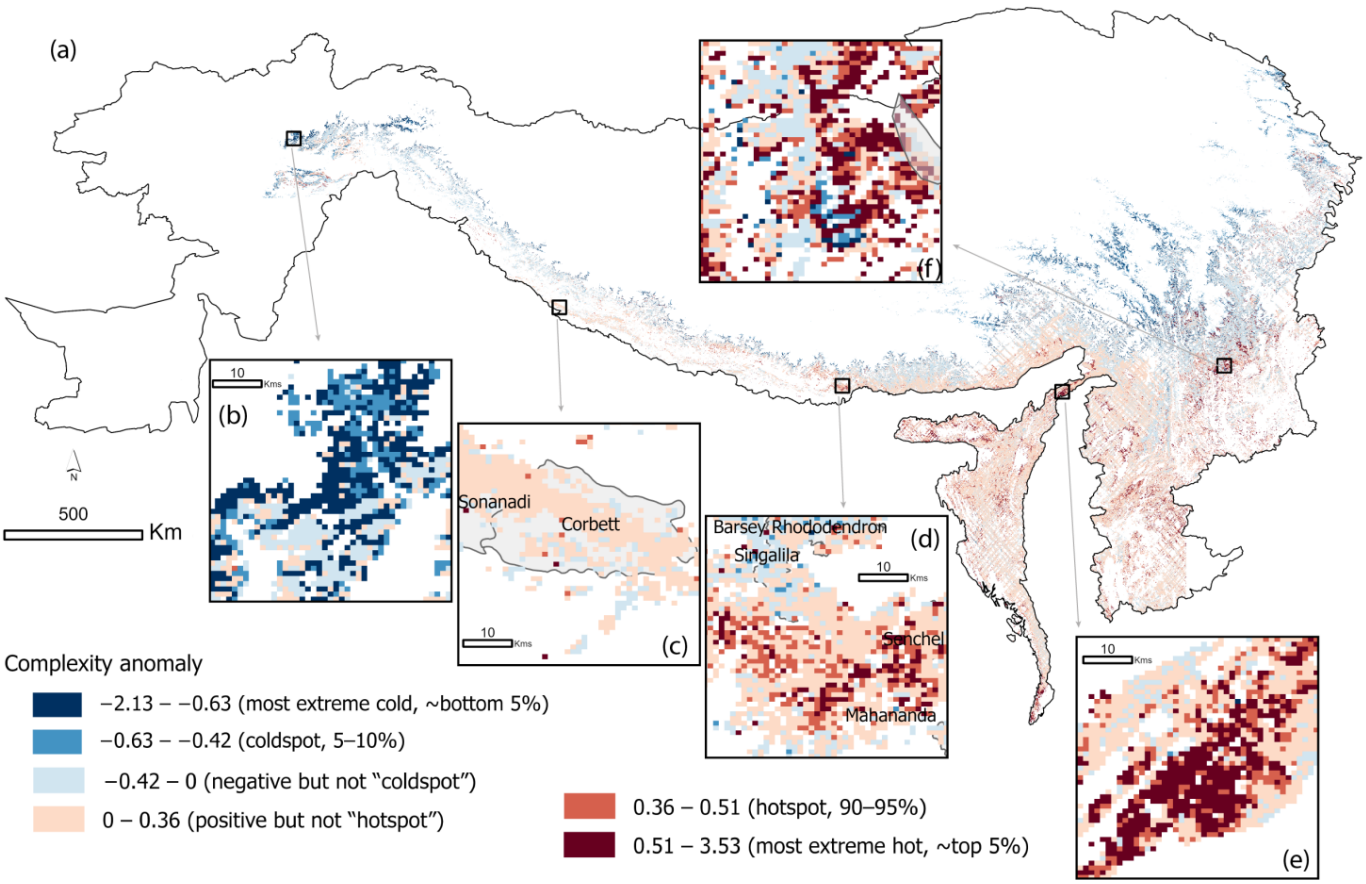

Figure 6. Spatial patterns of forest structural complexity anomalies ("indicator anomalies") across the HKH. (**a**) HKH-wide map of indicator anomalies. Insets (**b**–**f**) illustrate representative local-scale spatial structure and clustering of anomalies; labeled polygons indicate selected protected areas for geographic reference. This structural complexity anomaly can be accessed on the GEE platform at https://ee-nbm.projects.earthengine.app/view/wsci-anomaly-hkh2 (accessed on 6 March 2026).

Spatially, hotspots and coldspots show a strong geographic organization rather than random scatter. Using the structural complexity hotspot/coldspot class raster as a coarse spatial descriptor, hotspot pixels skew toward lower latitudes (median latitude ~25.6°N) and are concentrated farther east/southeast within the HKH domain (median longitude ~97.5°E), whereas coldspots are more frequent at higher latitudes (median ~30.8°N) and extend farther across the central/western arc (including much lower longitudes in the west). This pattern is consistent with the biogeographic and elevation stratifications below.

3.3.1. Elevation Structuring of Complexity Anomalies

Elevation-band summaries (200 m bins) show a strong, monotonic reorganization of structural complexity anomalies with height in the HKH (Figure 7). At lower elevations (≤1300 m), hotspots dominate and coldspots are rare: for example, at ~1100 m hotspots comprise ~14.5% of indicator coverage/footprint while coldspots are ~0.9%, and mean indicator anomaly is strongly positive (~+0.15). With increasing elevation, hotspot frequency steadily declines while coldspots rise, and the mean indicator anomaly weakens toward zero. The sign of mean indicator anomaly shifts from positive to negative between ~2100 and ~2300 m (i.e., the point where the height-normalized anomaly transitions from net "excess" to net deficit). Above mid-elevations, coldspots increase rapidly and increasingly dominate treeline-relevant belts: at ~3500 m hotspots drop to ~7.4% while coldspots rise to ~17.4% and the mean indicator anomaly is negative (~−0.13), further strengthening at

~4100 m. At the highest elevations sampled, coldspots become overwhelming, indicating that woody vegetation near and above upper-montane/treeline transition zones are consistently structurally simpler than expected for their canopy stature, whereas unexpectedly complex structure concentrates disproportionately in lower-elevation forests.

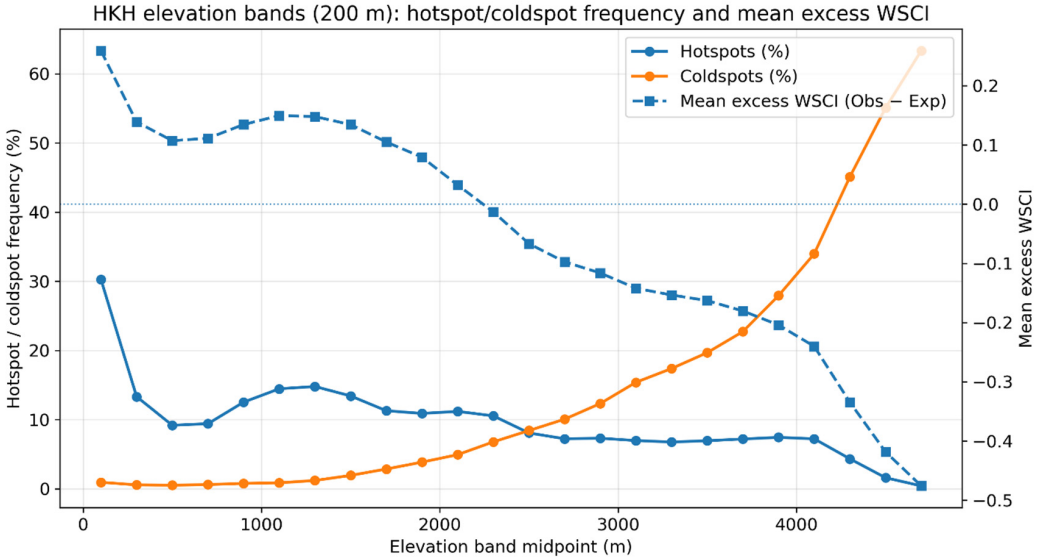

Figure 7. Hotspot and coldspot frequency by elevation and mean indicator anomaly complexity by elevation.

Furthermore, slope-class summaries based on mean SRTM-derived slope aggregated to the 1 km analysis grid showed a strong monotonic decline in indicator anomalies with increasing slope. Mean anomaly was positive in low-slope classes, crossed zero at approximately 25° mean slope, and became increasingly negative in steeper classes. Consistent with this pattern, structural complexity hotspot frequency declined sharply with slope, whereas coldspot frequency increased.

3.3.2. Structural Complexity Contrasts Among the Top Ecoregions

Stratifying the HKH trustable indicator footprint by biogeographic units revealed strong, coherent contrasts in the frequency of structural complexity anomalies among the dominant RESOLVE/WWF ecoregions (top 16 by masked-area coverage) (Figure 8). Overall, subtropical and tropical broadleaf systems exhibited a pronounced hotspot bias (positive indicator anomalies more common than negative), whereas alpine shrubland/meadow systems and several subalpine conifer ecoregions were coldspot-biased. The most hotspot-skewed ecoregions were Meghalaya subtropical forests (hotspots 38.2% vs. coldspots 2.8%; net +35.4%), Yunnan Plateau subtropical evergreen forests (28.7% vs. 4.2%; net +24.5%), and Northern Indochina subtropical forests (20.6% vs. 3.6%; net +17.0%). In contrast, the most coldspot-skewed ecoregions were Eastern Himalayan alpine shrub and meadows (1.0% vs. 31.8%; net −30.8%), Southeast Tibet shrublands and meadows (2.1% vs. 26.5%; net −24.4%), and Northeast Himalayan subalpine conifer forests (2.6% vs. 25.3%; net −22.7%). When aggregated to biome level, these patterns remained consistent: Tropical and Subtropical Moist Broadleaf Forests were strongly hotspot-biased (hot 17.6%, cold 4.0%), whereas Montane Grasslands and Shrublands were strongly coldspot-dominated (hot 2.4%, cold 25.9%). These results indicate that excess structural complexity is not evenly distributed across HKH woody landscapes but instead aligns with major biogeographic transitions, yielding ecoregion-specific “hot” and “cold” signatures in height-normalized complexity (Figure 8).

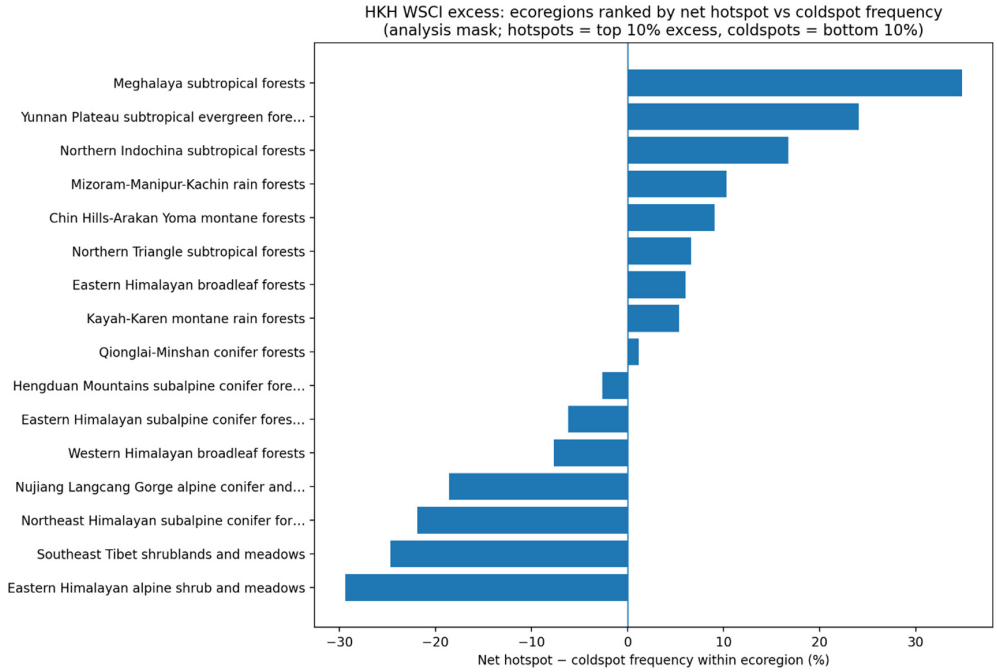

Figure 8. Ecoregions ranked by the net hotspot–coldspot frequency of WSCI excess. Positive values indicate ecoregions with a relative predominance of hotspots, whereas negative values indicate a predominance of coldspots.

3.3.3. Elevation + MAP–Controlled Ecoregion Contrasts in Hotspot and Coldspot Frequency

As ecoregions occupy different elevation and precipitation space, we then used stratified standardization to test whether ecoregion differences persist after removing these first-order compositional effects. After this elevation + MAP standardization, several ecoregions still depart systematically from expectation (Figure 9), indicating that biogeographic differences in anomaly frequency are not explained solely by where an ecoregion sits along the elevation and precipitation gradients. Some ecoregions show persistent hotspot enrichment (ObservedHot > ExpectedHot) accompanied by coldspot suppression (ObservedCold < ExpectedCold) (Figure 9a), implying that they contain more positive excess-complexity anomalies than would be predicted from their elevation–MAP composition alone. Conversely, a subset of ecoregions show the opposite pattern—hotspot deficits and coldspot enrichment—indicating a relative prevalence of negative anomalies even after controlling for elevation and precipitation (Figure 9b).

The Δhot–Δcold scatterplot (Figure 10) summarizes these departures as signed residuals (Observed − Expected) and organizes ecoregions into quadrants relative to the (0, 0) origin. Ecoregions in the (+Δhot, −Δcold) quadrant exhibit the clearest "excess-complexity" signal after adjustment—hotspots occur more frequently than expected while coldspots occur less frequently than expected—whereas ecoregions in the (−Δhot, +Δcold) quadrant exhibit a net "complexity deficit." Ecoregions plotting near the origin show little departure from the HKH baseline once elevation and precipitation are accounted for, suggesting that their anomaly frequencies are largely consistent with what would be expected from broad environmental composition. Importantly, the presence of ecoregions away from the origin indicates that biogeographic differences persist even after removing the dominant influence of elevation and precipitation, implying additional controls related to forest composition, disturbance regimes, land-use pressure, and/or protection effectiveness.

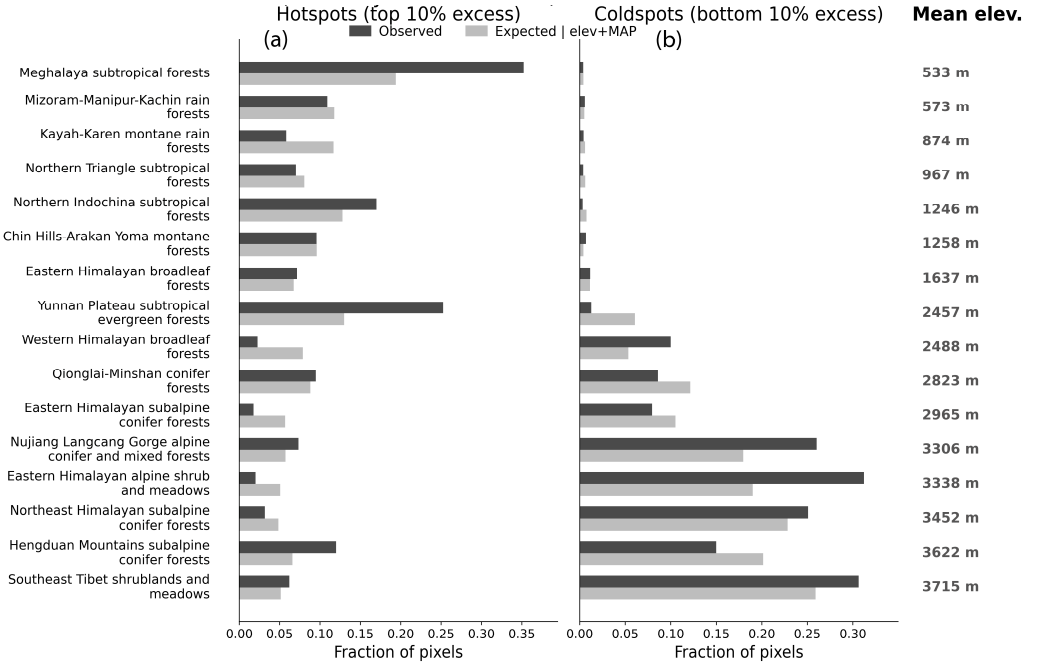

Figure 9. Elevation + MAP-controlled structural complexity hotspot/coldspot frequencies by ecoregion.

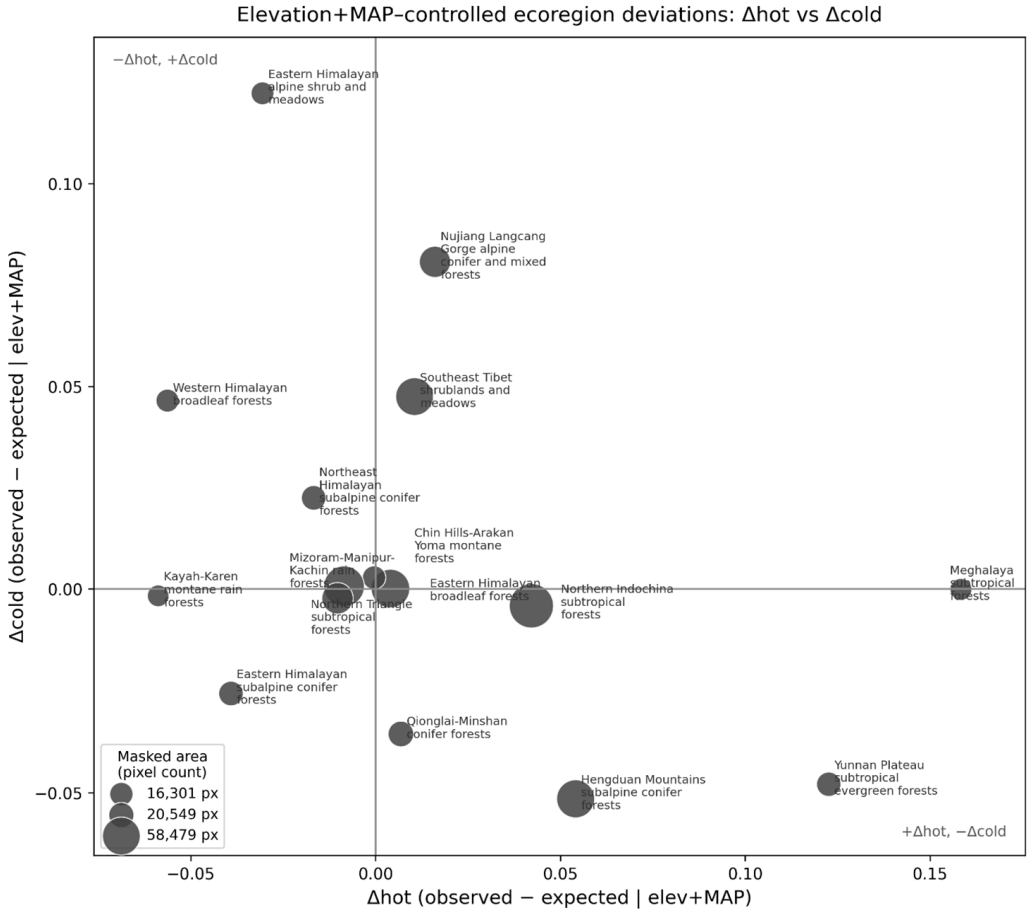

Figure 10. Elevation + MAP-controlled ecoregion deviations showing Δhot verses Δcold.

3.4. Protection: Inside vs. Outside Protected Areas

PAs intersecting HKH contained a substantial portion of the trustable forest footprint (pixels inside PAs within the analysis mask = 62,488). However, hotspot frequency was markedly lower inside protected areas than outside: inside-PAs hotspots were ~4.5% of PA pixels, compared to ~10.2% outside. Coldspot frequency was slightly lower inside (~9.2%) than outside (~10.4%), but the dominant protection signal was the sharp reduction in hotspot prevalence. Mean indicator anomaly was also more negative inside protected areas (inside ≈ -0.059 vs. outside ≈ -0.001), even though mean RH98 was higher inside PAs (inside ~27.2 m vs. outside ~23.1 m). This indicates that protected areas, as currently distributed across the HKH, are not preferentially associated with positive "excess complexity" relative to what canopy height would predict; instead, they tend to have lower-than-expected complexity. This pattern is consistent with a strong placement effect (PAs disproportionately located in high-elevation and less structurally diverse belts), which we further examine via elevation and ecoregion stratifications.

To reduce confounding by elevation, we repeated the protected-area comparison within 200 m elevation bands (1 km grid; SRTM-derived elevation aggregated to the analysis grid). Within the same elevation bands, protected-area pixels consistently exhibited fewer structural complexity anomalies than non-protected pixels. Hotspot frequency was lower inside protected areas in nearly every elevation band (22/23 bands), with a median within-band reduction of ~3–4 percentage points (Figure 11). Coldspot frequency was also generally lower inside protected areas (20/23 bands). Mean indicator anomaly (Observed − Expected) was slightly lower inside protected areas in most bands, indicating that protected forests tended to be closer to the HKH-wide height-normalized expectation. Together, these stratified results indicate that the protected-area signal is not driven solely by the elevational distribution of protected lands.

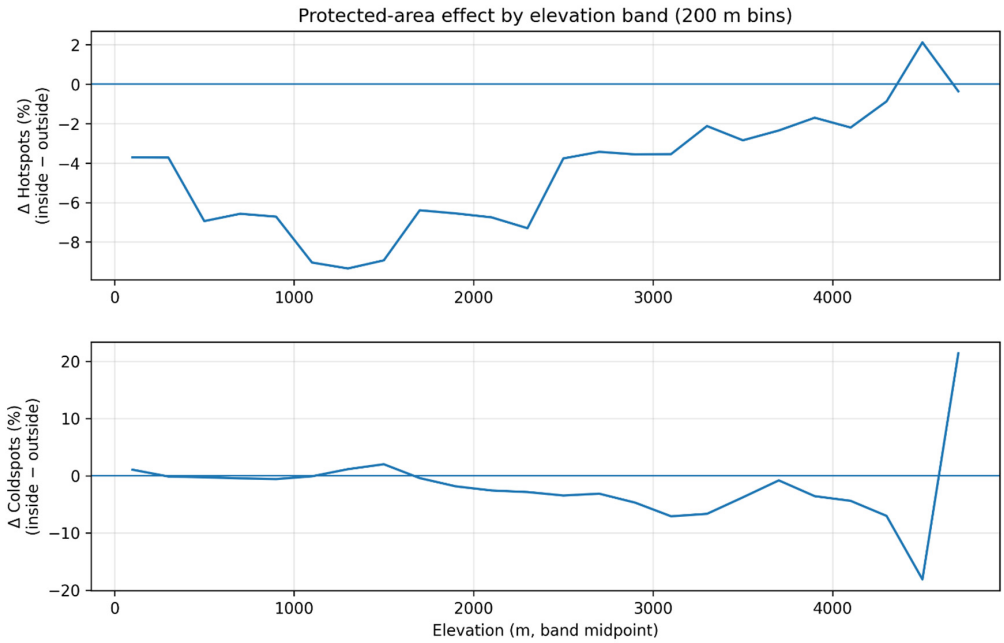

Figure 11. Protected area effect by elevation band.

4. Discussion

4.1. Interpreting Excess Complexity in Waveform Terms

The anomaly framework used in this study—indicator anomalies defined as the residual from the HKH-wide indicator baseline–height relationship—provides a way to interpret structural complexity that is not reducible to canopy height. In practice, positive

indicator anomalies indicate 1 km forested cells whose GEDI waveforms imply a more vertically distributed return profile than is typical for their canopy height, while negative excess indicates a more vertically concentrated profile than expected [24]. As WSCI is waveform-derived, it is sensitive to the shape of vertical energy distribution rather than any single height percentile [29]. Thus, excess complexity is plausibly associated with conditions that broaden or diversify the vertical return profile: Multi-layer canopies, mixed-stature stands, fine-scale gap structure and patchiness, and landscapes where successional stages are interwoven at sub-kilometer scales. Conversely, coldspots are consistent with comparatively "clean" vertical profiles, e.g., forests dominated by fewer strata, reduced sub-canopy signal, or structurally uniform stands that yield a narrower vertical distribution of returns for a given height. Importantly, these interpretations are relative: the residual is best treated as a height-normalized structural signal that enables comparison across strongly varying elevational and biogeographic settings in the HKH.

4.2. Beyond Elevation: Biogeographic and Hydroclimatic Controls After Adjustment

Elevation exerts first-order control on the spatial organization of woody vegetation in the HKH, and the elevation-belt analysis confirms strong elevation structure in structural complexity hotspot/coldspot frequencies. However, once we account for elevation (and, in the elevation + MAP control, the combined effects of elevation and mean annual precipitation), consistent departures among ecoregions remain. These elevation- and climate-adjusted differences suggest that structural complexity is also shaped by ecoregion-specific combinations of forest type, disturbance regime, and landscape configuration that are not fully captured by broad climatic templates.

Interpreting the adjusted ecoregion signal is therefore less about "wet equals complex" or "conifer equals simple," and more about how hydroclimate and temperature set the envelope within which additional mechanisms operate. For example, in ecoregions where adjusted hotspot rates remain high, one plausible interpretation is that canopy layering and vertical heterogeneity are promoted by compositional mixing (e.g., broadleaf–conifer mosaics), greater tree-species diversity and associated variation in crown architecture, recurring intermediate disturbance, or topographically driven patch dynamics (landslides, debris flows, wind disturbance) that create multi-cohort structure at scales detectable in 1 km waveform aggregates. Where adjusted coldspot tendencies persist, explanations may include structural constraint (short growing seasons, wind exposure), dominance by physiognomies with simpler vertical arrangements, or human-use legacies that simplify the understory and midstory while leaving the canopy height relatively intact. The key implication of the elevation + MAP control is that ecoregion contrasts are not merely "where forests are tall/wet," but reflect differences in how forests organize vertical structure under similar broad environmental conditions.

4.3. Protected Areas (PAs): Plausible Mechanisms, Confounding, and Interpretation Limits

The effects of PAs on height-normalized structural complexity in the HKH are not straightforward because WDPA polygons capture a wide range of governance and use contexts. Also, the placements of PAs are strongly patterned by accessibility and terrain. Consistent with site-selection bias, many PAs are concentrated in higher-elevation and steeper landscapes where forest stature, growing-season length, and disturbance regimes differ fundamentally from lower montane belts; therefore, simple inside–outside contrasts can conflate "protection" with location-specific factors [52]. Our results nonetheless show a clear empirical signal: within the trustable indicator footprint, hotspots of excess complexity are less frequent inside PAs than outside, and mean indicator anomaly is more negative inside PAs, even though mean canopy stature (RH98) is higher inside. Interpreted

conservatively, this pattern indicates that—at 1 km support—HKH protected lands are not systematically associated with greater-than-expected vertical complexity relative to height.

Several non-mutually exclusive mechanisms could produce this outcome. Fewer hotspots inside PAs may reflect differences in landscape configuration (e.g., fragmentation, successional mosaics, disturbance patchiness) that alter waveform vertical energy distribution at 1 km aggregation, rather than a direct 'benefit' or 'cost' of protection per se. Furthermore, in the HKH, PA status does not always guarantee greater structural complexity, as fuelwood removal, grazing, and other local resource use often persist inside protected boundaries, simplifying vertical structure even when canopy height remains largely intact [53,54]. Also, community-based forest management in HKH complicates simple PA comparisons because community forests often show gains in cover and biomass [55,56] without consistent increases in vertical complexity [7], meaning that WDPA boundaries and community-managed lands can follow different structural trajectories not fully captured by waveform metrics. While our within-elevation-band comparisons reduce the dominant elevational confounding, residual covariates likely remain (e.g., slope, aspect, accessibility, settlement proximity, historical land-use, and cross-border differences in management) [54,57]. Given these limitations, we interpret PA contrasts as associations that motivate more targeted follow-up (e.g., separating strict vs. multiple-use categories, incorporating accessibility proxies, or explicitly contrasting PAs with community-managed forests where boundaries are available), rather than as causal estimates of protection effects on complexity.

4.4. Methodological Considerations in the HKH: Sampling, Mixing, and Uncertainty

Several limitations are particularly relevant in the HKH. First, GEDI sampling is spatially uneven, and 1 km grid metrics depend on the number of contributing shots (countf). Our "Indicator coverage/footprint" mask (minimum RH98 and countf thresholds plus woody filtering) reduces the influence of sparse sampling, but it cannot fully eliminate sampling bias in areas with limited track coverage. Second, land-cover mixing is acute along sharp ecotones (e.g., treeline, shrublands, agroforestry mosaics) and in rugged terrain where 1 km cells can span large gradients in microclimate and canopy composition. This mixing can blur contrasts and can also produce apparently "valid" WSCI values in cells that are not dominantly woody unless an explicit woody/forest mask is applied. Third, uncertainty is heteroscedastic at large scales. The WSCI framework provides prediction-interval information that is intended to reflect spatially varying uncertainty, but a single global cutoff is unlikely to be appropriate across biomes and structural regimes. Our use of a percentile-based uncertainty cutoff (e.g., relPI p90) is therefore a pragmatic strategy. Nonetheless, uncertainty filtering remains a key sensitivity axis; reporting stability across p80–p95 style thresholds is important to demonstrate that structural complexity hotspot/coldspot patterns are not artifacts of the uncertainty mask.

4.5. Conservation and Monitoring Implications

The HKH is undergoing rapid environmental change, and conservation planning increasingly requires indicators that can be compared across countries and biogeographic zones [1]. In this context, this study contributes a repeatable, region-wide framework for identifying where forest vertical structure appears either unexpectedly complex or unexpectedly simplified. The resulting HKH-scale maps and stratified summaries offer practical guidance for conservation and management by highlighting areas where maintaining multi-layered canopies may be particularly important, where structural simplification could help guide restoration or targeted management interventions, and where ecotonal regions—such as treeline belts—exhibit anomalous structural patterns that warrant focused monitoring.

The structural anomaly atlas provides coherent basis for selecting candidate sentinel regions for field validation using terrestrial or handheld LiDAR and for tracking structural change over time as new GEDI acquisitions and updated data products become available. Our results also extend local Himalaya-focused structural complexity work—often based on plot/transect measurements [58] and increasingly on ground/airborne laser scanning [8,27]—by providing a first-order HKH-scale context in which those intensive observations can be embedded.

5. Conclusions

Using GEDI waveform LiDAR derived WSCI, this study produced the first HKH-scale, uncertainty-aware atlas of forest structural complexity anomalies. By defining a conservative trustable indicator footprint (woody cover, minimum GEDI sampling support and canopy-stature constraints, and a relative uncertainty filter), we limited inference to locations where gridded WSCI estimates are most defensible in a heterogeneous mountain landscape. A simple HKH-wide indicator baseline–height relationship enabled height-normalized interpretation through indicator anomalies (Observed − Expected), revealing coherent hotspot and coldspot patterning rather than random noise. Results show a strong elevational organization: hotspots concentrate in lower-elevation forests, while coldspots become increasingly dominant in upper-montane to treeline-relevant belts, consistent with progressively constrained vertical structure at high elevations. Ecoregions retain distinctive anomaly signatures even after controlling for elevation and mean annual precipitation, indicating additional biogeographic controls beyond broad climate gradients. Protected areas, as currently distributed, are not consistently associated with greater excess complexity and often show reduced hotspot prevalence, underscoring the importance of placement effects and the need for cautious interpretation. The anomaly framework provides a scalable way to move beyond canopy height toward region-wide hypotheses about disturbance, composition, and landscape configuration, and prioritize targeted field/UAV or terrestrial LiDAR validation in key ecoregions and elevation belts. Future work should also evaluate sensitivity to uncertainty thresholds, incorporate additional covariates and pursue footprint- or landscape-scale validation to better link waveform-derived anomalies to on-the-ground forest architecture and habitat function. To facilitate, the HKH forest complexity anomaly atlas is publicly available via GEE (https://ee-nbm.projects.earthengine.app/view/wsci-anomaly-hkh2, accessed on 6 March 2026).

Author Contributions: Conceptualization, N.B.M. and G.C.; methodology, N.B.M.; software, N.B.M.; validation, N.B.M.; formal analysis, N.B.M.; investigation, N.B.M. and G.C.; resources, N.B.M. and G.C.; data curation, N.B.M.; writing—original draft preparation, N.B.M.; writing—review and editing, N.B.M. and G.C.; visualization, N.B.M.; supervision, N.B.M. and G.C.; project administration, N.B.M. and G.C.; funding acquisition, N.B.M. and G.C. All authors have read and agreed to the published version of the manuscript.

Funding: N.B.M. was partially supported by Faculty Research Grant from University of Wisconsin-La Crosse.

Data Availability Statement: The HKH forest complexity anomaly atlas is publicly available via GEE (https://ee-nbm.projects.earthengine.app/view/wsci-anomaly-hkh2, accessed on 6 March 2026). The GEE scripts are available from the corresponding author on reasonable request.

Acknowledgments: N.B.M. thanks Paras Bikram Singh, Shalik Sigdel, Bharat Shrestha and Kumar Mainali for helpful discussions that informed the development and interpretation of this study. We also thank the GEDI mission team and the WSCI product developers for making GEDI observations and derived structural-complexity products openly available, and the Google Earth Engine team

for providing guidance and technical support that enabled HKH-scale analysis. We are grateful to the anonymous reviewers for constructive feedback that improved the clarity and robustness of the manuscript.

Conflicts of Interest: The authors declare no conflicts of interest.

References

1. Wester, P.; Mishra, A.; Mukherji, A.; Shrestha, A.B. *The Hindu Kush Himalaya Assessment: Mountains, Climate Change, Sustainability and People*; Springer Nature: Berlin/Heidelberg, Germany, 2019.
2. Areendran, G.; Sahana, M.; Raj, K.; Kumar, R.; Sivadas, A.; Kumar, A.; Deb, S.; Gupta, V.D. A systematic review on high conservation value assessment (HCVs): Challenges and framework for future research on conservation strategy. *Sci. Total Environ.* **2020**, *709*, 135425. [CrossRef] [PubMed]
3. Azam, M.F.; Kargel, J.S.; Shea, J.M.; Nepal, S.; Haritashya, U.K.; Srivastava, S.; Maussion, F.; Qazi, N.; Chevallier, P.; Dimri, A.; et al. Glaciohydrology of the Himalaya-Karakoram. *Science* **2021**, *373*, eabf3668. [CrossRef] [PubMed]
4. Joshi, A.; Joshi, P. Forest ecosystem services in the central Himalaya: Local benefits and global relevance. *Proc. Natl. Acad. Sci. India Sect. B Biol. Sci.* **2019**, *89*, 785–792. [CrossRef]
5. Xu, J.; Badola, R.; Chettri, N.; Chaudhary, R.P.; Zomer, R.; Pokhrel, B.; Hussain, S.A.; Pradhan, S.; Pradhan, R. Sustaining biodiversity and ecosystem services in the Hindu Kush Himalaya. In *The Hindu Kush Himalaya Assessment: Mountains, Climate Change, Sustainability and People*; Springer: Berlin/Heidelberg, Germany, 2019; pp. 127–165.
6. Rana, S.K.; Rawat, G.S. Database of Himalayan plants based on published floras during a century. *Data* **2017**, *2*, 36. [CrossRef]
7. Das, S.; Basnet, P.; Seidel, D.; Röll, A.; Ehbrecht, M.; Hölscher, D. Tree architecture and structural complexity in mountain forests of the Annapurna region, Himalaya. *Ecol. Evol.* **2025**, *15*, e71341. [CrossRef]
8. Basnet, P.; Das, S.; Hölscher, D.; Pierick, K.; Seidel, D. Drivers of Forest Structural Complexity in Mountain Forests of Nepal. *Mt. Res. Dev.* **2025**, *45*, R1–R10. [CrossRef]
9. McElhinny, C.; Gibbons, P.; Brack, C.; Bauhus, J. Forest and woodland stand structural complexity: Its definition and measurement. *For. Ecol. Manag.* **2005**, *218*, 1–24. [CrossRef]
10. Ehbrecht, M.; Schall, P.; Ammer, C.; Seidel, D. Quantifying stand structural complexity and its relationship with forest management, tree species diversity and microclimate. *Agric. For. Meteorol.* **2017**, *242*, 1–9. [CrossRef]
11. Gough, C.M.; Atkins, J.W.; Fahey, R.T.; Hardiman, B.S. High rates of primary production in structurally complex forests. *Ecology* **2019**, *100*, e02864. [CrossRef] [PubMed]
12. Coverdale, T.C.; Davies, A.B. Unravelling the relationship between plant diversity and vegetation structural complexity: A review and theoretical framework. *J. Ecol.* **2023**, *111*, 1378–1395. [CrossRef]
13. Gough, C.M.; Atkins, J.W.; Bond-Lamberty, B.; Agee, E.A.; Dorheim, K.R.; Fahey, R.T.; Grigri, M.S.; Haber, L.T.; Mathes, K.C.; Pennington, S.C.; et al. Forest structural complexity and biomass predict first-year carbon cycling responses to disturbance. *Ecosystems* **2021**, *24*, 699–712. [CrossRef]
14. Liang, M.; González-Roglich, M.; Roehrdanz, P.; Tabor, K.; Zvoleff, A.; Leitold, V.; Silva, J.; Fatoyinbo, T.; Hansen, M.; Duncanson, L. Assessing protected area's carbon stocks and ecological structure at regional-scale using GEDI lidar. *Glob. Environ. Change* **2023**, *78*, 102621. [CrossRef]
15. Lešo, P.; Wyka, J.; Korňan, M.; Horák, J.; Kropil, R.; Lešová, A.; Kusal, B.; Kajtoch, Ł. Forest management in mountain mixed forests has moderate impact on breeding bird assemblages, but it substantially decreases the diversity of rare taxa. *For. Ecol. Manag.* **2025**, *597*, 123123. [CrossRef]
16. Atkins, J.W.; Walter, J.A.; Stovall, A.E.; Fahey, R.T.; Gough, C.M. Power law scaling relationships link canopy structural complexity and height across forest types. *Funct. Ecol.* **2022**, *36*, 713–726. [CrossRef]
17. Hansen, A.J.; Phillips, L.B.; Dubayah, R.; Goetz, S.; Hofton, M. Regional-scale application of lidar: Variation in forest canopy structure across the southeastern US. *For. Ecol. Manag.* **2014**, *329*, 214–226. [CrossRef]
18. Asner, G.; Anderson, C.; Martin, R.; Knapp, D.; Tupayachi, R.; Sinca, F.; Malhi, Y. Landscape-scale changes in forest structure and functional traits along an Andes-to-Amazon elevation gradient. *Biogeosciences* **2014**, *11*, 843–856. [CrossRef]
19. Khanal, S.; Nolan, R.H.; Medlyn, B.E.; Boer, M.M. Topoclimatic factors create favourable conditions for carbon-dense forests in the Central Himalayas. *Sci. Rep.* **2025**, *15*, 35134. [CrossRef] [PubMed]
20. Jia, J.; Hughes, A.C.; Nunes, M.H.; Santos, E.G.; Pellikka, P.K.; Kalliovirta, L.; Maeda, E.E. Forest structural and microclimatic patterns along an elevational gradient in Mount Kenya. *Agric. For. Meteorol.* **2024**, *356*, 110188. [CrossRef]
21. Ahmad, A.; Sastry, S.; Dhakal, A.; Khanal, S.; Levering, A.; Gilani, H.; Jacobs, N. Canopy height mapping in the Western Himalayas, Pakistan: A deep learning approach using GEDI and Sentinel-2 fusion. *Int. J. Appl. Earth Obs. Geoinf.* **2026**, *146*, 105030. [CrossRef]

22. Mishra, N.B.; Mainali, K.P. Greening and browning of the Himalaya: Spatial patterns and the role of climatic change and human drivers. *Sci. Total Environ.* **2017**, *587*, 326–339. [CrossRef]
23. Hansen, M.C.; Potapov, P.V.; Moore, R.; Hancher, M.; Turubanova, S.A.; Tyukavina, A.; Thau, D.; Stehman, S.V.; Goetz, S.J.; Loveland, T.R. High-resolution global maps of 21st-century forest cover change. *Science* **2013**, *342*, 850–853. [CrossRef] [PubMed]
24. de Conto, T.; Armston, J.; Dubayah, R. Characterizing the structural complexity of the Earth's forests with spaceborne lidar. *Nat. Commun.* **2024**, *15*, 8116. [CrossRef]
25. Zhang, X.; Friedl, M.A.; Schaaf, C.B. Global vegetation phenology from Moderate Resolution Imaging Spectroradiometer (MODIS): Evaluation of global patterns and comparison with in situ measurements. *J. Geophys. Res. Biogeosci.* **2006**, *111*, G04017. [CrossRef]
26. Verbesselt, J.; Hyndman, R.; Zeileis, A.; Culvenor, D. Phenological change detection while accounting for abrupt and gradual trends in satellite image time series. *Remote Sens. Environ.* **2010**, *114*, 2970–2980. [CrossRef]
27. Mishra, N.B.; Singh, P.B. Reading the Himalayan Treeline in 3D: Species Turnover and Structural Thresholds from UAV LiDAR. *Remote Sens.* **2026**, *18*, 309. [CrossRef]
28. Dong, P.; Chen, Q. *LiDAR Remote Sensing and Applications*; CRC Press: Boca Raton, FL, USA, 2017.
29. Dubayah, R.; Blair, J.B.; Goetz, S.; Fatoyinbo, L.; Hansen, M.; Healey, S.; Hofton, M.; Hurtt, G.; Kellner, J.; Luthcke, S.; et al. The Global Ecosystem Dynamics Investigation: High-resolution laser ranging of the Earth's forests and topography. *Sci. Remote Sens.* **2020**, *1*, 100002. [CrossRef]
30. Potapov, P.; Li, X.; Hernandez-Serna, A.; Tyukavina, A.; Hansen, M.C.; Kommareddy, A.; Pickens, A.; Turubanova, S.; Tang, H.; Silva, C.E.; et al. Mapping global forest canopy height through integration of GEDI and Landsat data. *Remote Sens. Environ.* **2021**, *253*, 112165. [CrossRef]
31. Dubayah, R.; Armston, J.; Healey, S.P.; Bruening, J.M.; Patterson, P.L.; Kellner, J.R.; Duncanson, L.; Saarela, S.; Ståhl, G.; Yang, Z.; et al. GEDI launches a new era of biomass inference from space. *Environ. Res. Lett.* **2022**, *17*, 095001. [CrossRef]
32. De Conto, T.; Armston, J.; Dubayah, R. *GEDI L4C Footprint Level Waveform Structural Complexity Index, Version 2*; ORNL DAAC: Oak Ridge, TN, USA, 2024.
33. East, A.; Hansen, A.; Jantz, P.; Currey, B.; Roberts, D.W.; Armenteras, D. Validation and error minimization of global ecosystem dynamics investigation (GEDI) relative height metrics in the Amazon. *Remote Sens.* **2024**, *16*, 3550. [CrossRef]
34. Mishra, N.B.; Singh, P.B. Mountains of error: UAV LiDAR benchmarking of GEDI and GEDI-derived global canopy height products in steep Himalayan forests. *Int. J. Appl. Earth Obs. Geoinf.* **2026**, *147*, 105203. [CrossRef]
35. You, Q.-L.; Ren, G.-Y.; Zhang, Y.-Q.; Ren, Y.-Y.; Sun, X.-B.; Zhan, Y.-J.; Shrestha, A.B.; Krishnan, R. An overview of studies of observed climate change in the Hindu Kush Himalayan (HKH) region. *Adv. Clim. Change Res.* **2017**, *8*, 141–147. [CrossRef]
36. Singh, J.; Singh, S.P. Forest vegetation of the Himalaya. *Bot. Rev.* **1987**, *53*, 80–192. [CrossRef]
37. Dimri, A.; Niyogi, D.; Barros, A.; Ridley, J.; Mohanty, U.; Yasunari, T.; Sikka, D. Western disturbances: A review. *Rev. Geophys.* **2015**, *53*, 225–246. [CrossRef]
38. Dhyani, S. Are Himalayan ecosystems facing hidden collapse? Assessing the drivers and impacts of change to aid conservation, restoration and conflict resolution challenges. *Biodivers. Conserv.* **2023**, *32*, 3731–3764. [CrossRef]
39. Chen, T.-H.K.; Pandey, B.; Seto, K.C. Detecting subpixel human settlements in mountains using deep learning: A case of the Hindu Kush Himalaya 1990–2020. *Remote Sens. Environ.* **2023**, *294*, 113625. [CrossRef]
40. Chaudhary, S.; Uddin, K.; Chettri, N.; Thapa, R.; Sharma, E. Protected areas in the Hindu Kush Himalaya: A regional assessment of the status, distribution, and gaps. *Conserv. Sci. Pract.* **2022**, *4*, e12793. [CrossRef]
41. Kotru, R.K.; Shakya, B.; Joshi, S.; Gurung, J.; Ali, G.; Amatya, S.; Pant, B. Biodiversity conservation and management in the Hindu Kush Himalayan Region: Are transboundary landscapes a promising solution? *Mt. Res. Dev.* **2020**, *40*, A15. [CrossRef]
42. Adler, C.; Wester, P.; Bhatt, I.; Huggel, C.; Insarov, G.; Morecroft, M.; Muccione, V.; Prakash, A.; Alcántara-Ayala, I.; Allen, S.K.; et al. Cross-chapter paper 5: Mountains. In *Climate Change 2022: Impacts, Adaptation, and Vulnerability*; IPCC: Geneva, Switzerland, 2023.
43. Krishnan, R.; Shrestha, A.B.; Ren, G.; Rajbhandari, R.; Saeed, S.; Sanjay, J.; Syed, M.A.; Vellore, R.; Xu, Y.; You, Q.; et al. Unravelling climate change in the Hindu Kush Himalaya: Rapid warming in the mountains and increasing extremes. In *The Hindu Kush Himalaya Assessment: Mountains, Climate Change, Sustainability and People*; Springer: Berlin/Heidelberg, Germany, 2019; pp. 57–97.
44. Vaidya, R.A.; Shrestha, M.S.; Nasab, N.; Gurung, D.R.; Kozo, N.; Pradhan, N.S.; Wasson, R.J. Disaster risk reduction and building resilience in the Hindu Kush Himalaya. In *The Hindu Kush Himalaya Assessment: Mountains, Climate Change, Sustainability and People*; Springer: Berlin/Heidelberg, Germany, 2019; pp. 389–419.
45. De Conto, T.; Armston, J.; Dubayah, R. *GEDI L4C Gridded Waveform Structural Complexity Index, Version 2*; ORNL DAAC: Oak Ridge, TN, USA, 2025.
46. Burns, P.; Hakkenberg, C.R.; Goetz, S.J. Multi-resolution gridded maps of vegetation structure from GEDI. *Sci. Data* **2024**, *11*, 881. [CrossRef]

47. Olson, D.M.; Dinerstein, E.; Wikramanayake, E.D.; Burgess, N.D.; Powell, G.V.; Underwood, E.C.; D'amico, J.A.; Itoua, I.; Strand, H.E.; Morrison, J.C.; et al. Terrestrial Ecoregions of the World: A New Map of Life on Earth: A new global map of terrestrial ecoregions provides an innovative tool for conserving biodiversity. *Bioscience* **2001**, *51*, 933–938. [CrossRef]
48. Bingham, H.C.; Juffe Bignoli, D.; Lewis, E.; MacSharry, B.; Burgess, N.D.; Visconti, P.; Deguignet, M.; Misrachi, M.; Walpole, M.; Stewart, J.L.; et al. Sixty years of tracking conservation progress using the World Database on Protected Areas. *Nat. Ecol. Evol.* **2019**, *3*, 737–743. [CrossRef] [PubMed]
49. Yang, L.; Meng, X.; Zhang, X. SRTM DEM and its application advances. *Int. J. Remote Sens.* **2011**, *32*, 3875–3896. [CrossRef]
50. Gorelick, N.; Hancher, M.; Dixon, M.; Ilyushchenko, S.; Thau, D.; Moore, R. Google Earth Engine: Planetary-scale geospatial analysis for everyone. *Remote Sens. Environ.* **2017**, *202*, 18–27. [CrossRef]
51. Hijmans, R.J.; Cameron, S.E.; Parra, J.L.; Jones, P.G.; Jarvis, A. Very high resolution interpolated climate surfaces for global land areas. *Int. J. Climatol.* **2005**, *25*, 1965–1978. [CrossRef]
52. Joppa, L.N.; Pfaff, A. High and far: Biases in the location of protected areas. *PLoS ONE* **2009**, *4*, e8273. [CrossRef]
53. Padmawathe, R.; Qureshi, Q.; Rawat, G. Effects of selective logging on vascular epiphyte diversity in a moist lowland forest of Eastern Himalaya, India. *Biol. Conserv.* **2004**, *119*, 81–92. [CrossRef]
54. Pandit, M.; Sodhi, N.S.; Koh, L.P.; Bhaskar, A.; Brook, B.W. Unreported yet massive deforestation driving loss of endemic biodiversity in Indian Himalaya. *Biodivers. Conserv.* **2007**, *16*, 153–163. [CrossRef]
55. Rawal, K.; Subedi, P.B. Vegetation structure and carbon stock potential in the community-managed forest of the mid-western hilly region, Nepal. *Asian J. For.* **2022**, *6*, 15–21. [CrossRef]
56. Pandey, H.P.; Maaren, I.E.; Shah, K.K.; Maraseni, T.N. Response of topographic and biodiversity variables on biomass and carbon density in community forests of Himalayan foot-hills. *J. For. Livelihood* **2020**, *19*, 51–65.
57. Måren, I.E.; Sharma, L.N. Managing biodiversity: Impacts of legal protection in mountain forests of the Himalayas. *Forests* **2018**, *9*, 476. [CrossRef]
58. Yadav, B.K.; Bhatta, K.P.; Ayer, S.; Basnet, P.; Dhakal, N.; Sharma, S.; Kadariya, R.; Bhandari, S.K. Elevation Shapes Tree Composition, Structure and Diversity More Than Soil Properties in the Annapurna Conservation Area, Nepal. *Trees For. People* **2025**, *20*, 100902. [CrossRef]

Disclaimer/Publisher's Note: The statements, opinions and data contained in all publications are solely those of the individual author(s) and contributor(s) and not of MDPI and/or the editor(s). MDPI and/or the editor(s) disclaim responsibility for any injury to people or property resulting from any ideas, methods, instructions or products referred to in the content.